Proceedings of The Research Institute of Atmospherics,
Nagoya University, Vol. 18 (1971)

IMAGE CORRECTION IN HIGH-RESOLUTION RADIO INTERFEROMETER

Masato ISHIGURO

Abstract

One of difficulties in a high-resolution multi-element interferometer system is the maintenance of phase relations between the antenna elements.

It is shown here that this difficulty can be overcome by introducing digital data processing, in which the image of the sun is corrected from the viewpoint of the spatial frequency characteristics of an antenna.

Further, a new configuration of the interferometer for phase orror correction is proposed.

1. Introduction

The brightness distribution of the source is given by the angular spectrum on the celestial sphere. If the antenna beam scans the source, or the source drifts across the antenna beam, the spatial brightness distribution is transformed into a waveform as a function of time. But, this waveform is the result of various kind of transformations which the signal has encountered between the source and the observer. These are: propagation effects, such as scintillation; spatial frequency characteristics of antennas; transmission characteristics of the receiving system; and so on.

Above all, the second transformation is the most important for the mapping of the radio source. The last one is also important in high-resolution systems. The theory of an antenna as a spatial frequency filter was first investigated by Bracewell and Roberts (1954). The spatial frequency characteristic of an antenna is determined by the complex auto-correlation function of the antenna aperture illumination. For a finite aperture antenna, its transfer function is band-limited and is zero for frequencies above the cutoff frequency which corresponds to the resolving power. The

observed image is obtained as the result of the convolution of the original brightness distribution with the mirror image of the antenna power pattern. So it is important to find effective methods of restoring the original brightness distribution from the observed data. Some theoretiacal treatments about the restoration have been proposed (Bracewell and Roberts, 1954; Bracewell, 1958; Ksienski, 1963; Burr, 1954), but few experimental examples (Peterson, 1969) have been reported.

The spatial frequency characteristics of an interferometer are represented by a set of equally-spaced line spectra, provided each antenna element tracks the radio soure. This character is very convenient for the digital processing of the observed data in the spatial frequency domain.

At Toyokawa, two (32+2)-element compound interferometers for solar observations at 3.75 GHz and 9.4 GHz have been in operation since 1967 and 1966 respectively (Tanaka et al. 1967, 1969). A general view of the compound interferometer is shown in Fig. 1.

It is shown here that the observations can be made more reliable by comparing the two different types of solar scans, one coming from the 32-element adding interferometer and the other from the (32+2)-element compound interforemeter. The former is inferior to the latter in resolving power, but the situation reverses for tolerance to phase error.

Since digital processing is available, it has been possible to get an improved radio map of the sun, by making the most of both merits.

Another use of combining the two systems is also discussed. In the solar scan data of the 9.4 GHz compound interferometer the fundamental Fourier component is missing, but it can be restored by that from the adding interferometer.

Finally it should be mentioned that the processing time has been greatly reduced by the use of the Fast Fourier Transform Algorithm (Cooley and Turkey, 1965), which has made the processing quite practical.

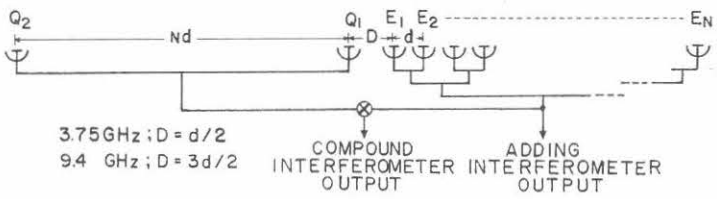

Fig. 1. General view of the compound interferometer.

2. Spatial Frequency Characteristics of an Interferometer

In following discussions we consider, for simplicity, the case when radio sources are incoherent and the cutoff frequency of the ordinary filter is much wider than

that of the spatial frequency filter.

If there are phase errors along the antenna aperture, the excitation coefficients of the antenna elements must be considered as complex quantities.

Let them be, $E_1, E_2, \ldots, E_N$ for the N-element basic interferometer and Q_1, Q_2 for the auxiliary 2-element interferometer. Then,

$$E_1=A_1 \exp(j\phi_1),\ E_2=A_2 \exp(j\phi_2),\ \ldots,\ E_N=A_N \exp(j\phi_N) \cdots\cdots (1)$$

$$Q_1=B_1 \exp(j\psi_1),\ Q_2=B_2 \exp(j\psi_2) \cdots\cdots (2)$$

where, $A_1, A_2, \ldots, A_N, B_1, B_2$ represent the nonuniformity between gains of unit paraboloid and losses of transmission lines, and $\phi_1, \phi_2, \ldots, \phi_N, \psi_1, \psi_2$ represent the phase errors of transmission lines.

2. 1 *The N-element adding interferometer*

From the geometrical configuration, the aperture illumination of the N-element adding interferometer is easily shown using Dirac's delta function as follows,

$$E^+(s) = \sum_{n=1}^{N} E_n\, \delta\,[s-(n-1)\,d_\lambda] \cdots\cdots (3)$$

where, $s = x/\lambda$ and $d_\lambda = d/\lambda$ (See Appendix).

From Eq. (3) and Eq. (A−1), the far-field pattern is

$$E^+(u) = \sum_{n=1}^{N} E_n \exp(j\,2\pi(n-1)\,d_\lambda\,u] \cdots\cdots (4)$$

From Eq. (3) and Eq. (A−4), the spatial frequency characteristics of the N-element adding interferometer are given by

$$\begin{aligned} P^+(s) &= \int_{-\infty}^{\infty} \sum_{n=1}^{N} E_n\,\delta\,[s'+s-(n-1)\,d_\lambda] \cdot \sum_{m=1}^{N} E_m^*\,\delta\,[s'-(m-1)\,d_\lambda]\,ds' \\ &= \sum_{n=1}^{N}\sum_{m=1}^{N} E_n\,E_m^*\,\delta\,[s-(n-m)\,d_\lambda] \\ &= s_0^+\,\delta(s) + \sum_{k=1}^{N-1}[s_{-2k}^+\,\delta(s+2k\sigma) + s_{2k}^+\,\delta(s-2k\sigma)] \cdots\cdots (5) \end{aligned}$$

where,

$$s_{2k}^+ = \sum_{m=1}^{N-k} E_{m+k}\,E_m^* \cdots\cdots (6)$$

and

$$s^{+}_{-2k} = s^{+*}_{2k} \quad \cdots\cdots (7)$$

for $k = 0, 1, 2, \ldots, N-1$.

The fundamental frequency σ is chosen to be $d/2$ for the future convenience.

From Eq. (5) and Eq. (A−11) the spatial frequency spectrum of the brightness distribution observed with the N-element adding interferometer is

$$T^{+}_{a}(s) = \sum_{k=1-N}^{N-1} s^{+}_{2k}\, \delta(s-2k\sigma)\, T(s)$$

$$= T^{+}_{a}(0)\,\delta(s) + \sum_{k=1}^{N-1} [T^{+}_{a}(-2k\sigma)\,\delta(s+2k\sigma) + T^{+}_{a}(2k\sigma)\,\delta(s-2k\sigma)] \quad \cdots\cdots (8)$$

where,

$$T^{+}_{a}(2k\sigma) = s^{+}_{2k} \cdot T(2k\sigma) \quad \cdots\cdots (9)$$

and

$$T^{+}_{a}(-2k\sigma) = T^{+}_{a}(2k\sigma)^{*} \quad \cdots\cdots (10)$$

for $k = 0, \pm 1, \pm 2, \ldots, \pm(N-1)$.

Spatial Fourier components of Eq. (9) and Eq. (10) are given by the Fourier transform of the observed waveform. These relationships are uncertain especially at higher spatial frequencies, when the S/N ratio of the receiver circuit is poor.

2. 2 *The (N+2)-element compound interferometer*

First, we consider the case when $D = d/2$ in Fig. 1. If we choose the position of Q_1 as the origin of the coordinate, the aperture illumination of the N-element basic interferometer is

$$E_A(s) = \sum_{n=1}^{N} E_1\, \sigma[s-(2n-1)\sigma], \quad \cdots\cdots (11)$$

and that of the auxiliary 2-element interferometer is

$$E_B(s) = Q_1\,\delta(s) + Q_2\,\delta(s+2N\sigma). \quad \cdots\cdots (12)$$

Then, the spatial frequency characteristics of the (N+2)-element compound interferometer are given by

$$P^x(s) = (1/2)\int_{-\infty}^{\infty} [E_A(s'+s)\,E_B(s')^* + E_B(s'+s)\,E_A(s')^*]\,ds'$$

$$= (1/2)\sum_{n=1}^{N} \{E_n^*\,Q_1\,\delta[s+(2n-1)\sigma] + E_n^*\,Q_2\,\delta[s+(2N+2n-1)\sigma]$$

$$+ E_n\,Q_1^*\,\delta[s-(2n-1)\sigma] + E_n^*\,Q_2\,\delta[s-(2N+2n-1)\sigma]\}$$

$$= \sum_{k=1}^{2N} \{s^x_{1-2k}\,\delta[s+(2k-1)\sigma] + s^x_{2k-1}\,\delta[s-(2k-1)\sigma]\} \quad \cdots\cdots (13)$$

where,

$$s^x_{2k-1} = \begin{cases} E_k\,Q_1^* & \text{for } 1 \leqq k \leqq N \quad \cdots\cdots (14) \\ E_{k-N}\,Q_2^* & \text{for } N+1 \leqq k \leqq 2N \quad \cdots\cdots (15) \end{cases}$$

and

$$s^x_{1-2k} = s^{x*}_{2k-1}. \quad \cdots\cdots (16)$$

From Eq. (13) and Eq. (A−11) the spatial frequency spectrum of the brightness distribution observed with the (N+2)-element compound interferometer is

$$T_a^x(s) = \sum_{k=1}^{2N} \{s^x_{1-2k}\,\delta[s+(2k-1)\sigma] + s^x_{2k-1}\,\delta[s-(2k-1)\sigma]\}\,T(s)$$

$$= \sum_{k=1}^{2N} \{T_a^x[(1-2k)\sigma]\,\delta[s+(2k-1)\sigma] + T_a^x[(2k-1)\sigma]\,\delta[s-(2k-1)\sigma]\}$$

$$\cdots\cdots (17)$$

where,

$$T_a^x[(2k-1)\sigma] = s^x_{2k-1} \cdot T[(2k-1)\sigma] \quad \cdots\cdots (18)$$

and

$$T_a^x[(1-2k)\sigma] = T_a^x[(2k-1)\sigma]^* \quad \cdots\cdots (19)$$

for $k=1, 2, \ldots, 2N$ (when $D=3d/2$, $k=2, 3, \ldots, 2N+1$)

2. 3 *Theory of phase correction*

Eq. (8) and Eq. (17) show that the spatial frequency spectrum of the observed brightness distribution contains only even harmonics for the adding interferometer and only odd harmonics for the compound interferometer. So, it is impossible to compare the spatial Fourier components directly.

But, if T(u) is the truncated function in the u-domain, the odd harmonics are interpolated from the even harmonics, and *vice versa*. This is well known as the sampling theorem for the frequency domain. Thus,

$$T[(2k-1)\sigma] = \sum_{i=-\infty}^{\infty} T(2i\sigma) \frac{\sin[2k-2i-1)\pi/2]}{(2k-2i-1)\pi/2} . \quad \cdots\cdots (20)$$

Substituting Eq. (9) and Eq. (18) into Eq. (20), we have

$$\frac{T_a^x[(2k-1)\sigma]}{s_{2k-1}^x} = \sum_{i=1-N}^{N-1} \frac{T_a^+(2k\sigma)}{s_{2k}^+} \frac{\sin[(2k-2i-1)\pi/2]}{(2k-2i-1)\pi/2} . \quad \cdots\cdots (21)$$

Supposing that elements Q_1 and E_1 in Fig. 1 are phase-locked (i. e., $\psi_1 = \phi_1 = 0$), and have an equal gain of 1 (i. e., $B_1 = A_1 = 1$), unknown parameters in the antenna aperture of interferometer are $E_2, E_3, \ldots, E_N$.

Then, Eq. (21) is the form of simultaneous equations which determine these parameters. If these can be solved uniquely, it is possible to restore the spatial frequency spectrum of the original brightness distribution. We have not yet found any direct method of solving Eq. (17). So, in the next section an approximation is introduced for the phase correction procedure, in which we assume there are no phase errors in the spatial frequency spectrum of the brightness distribution observed with adding interferometer. This assumption is reasonable for lower spatial frequency region where each Fourier component is produced by many pairs of antennas. With an additional assumption that all the antenna elements have equal gain (i. e., $A_1 = A_2 = \ldots = A_N = 1$), the spatial frequency characteristics of N-element adding interferometer is approximated from Eq. (6) as follows,

$$s_{2k}^+ = (N-k)/N \quad \cdots\cdots (22)$$

for $k = 1, 2, \ldots, N-1$.

Then, the odd Fourier components interpolated from $T_a^+(2k)$ after emphasizing

higher Fourier components are given by

$$T_a^{+x}[(2k-1)\sigma] = \sum_{i=1-N}^{N-1} \frac{T_a^{+}(2k\sigma)}{(N-k)/N} \frac{\sin[(2k-2i-1)\pi/2]}{(2k-2i-1)\pi/2} \cdots (23)$$

for k=1, 2, ..., N−1. Inverse Fourier transform of Eq. (23) gives a restored brightness distribution $T_a^{+x}(u)$, in which we can see more sharpend distribution.

The phase of $T_a^{+x}[(2k-1)\sigma]$ is more reliable than that of $T_a^{x}[(2k-1)\sigma]$, but the amplitude is not. Because, when there are phase errors the approximation of Eq. (22) is not correct.

So, the most reasonable method of correction for $T_a^{x}[(2k-1)\sigma]$ may be to substitute the phase of $T_a^{+x}[(2k-1)\sigma]$ for that of $T_a^{x}[(2k-1)\sigma]$ with its amplitude remaining unchanged. The phase difference between the above two spectra means the phase of s_{2k-1}^{x}, i. e. $(\phi_k - \psi_1)$. Then, it is possible to estimate to some extent the phase error distribution along the antenna aperture.

But, the higher the spatial frequency is, the more inaccurate this estimation become, because in adding interferometer the tolerance to the phase error decreases with spatial frequency.

When D=3d/2 in Fig. 1, the above mentioned procedure is applicable in quite the same mammer except for the fundamental spatial Fourier component.

This is restored from $T_a^{+x}(\sigma)$ after multiplying by some complex scaling factor which produces best agreement between the twe spatial frequency spectra.

The smoothing of $T_a^{x}(u)$ is performed by the method of T. H. Legg (1964) as follows,

$$\overline{T}_a^{x}(u) = [0.42T_a^{x}(u-u_0) + T_a^{x}(u) + 0.42\,T_a^{x}(u+u_0)]/1.84 \cdots\cdots (24)$$

where, $u_0 = 1/4Nd$, and the bar on $T_a^{x}(u)$ represents a smoothed value.

The effect of this in the spatial frequency domain is considered for the low pass filter, the characteristic of which is,

$$H[(2k-1)\sigma] = [1+0.84\cos(2k-1)\pi/4N]/1.84. \cdots\cdots\cdots\cdots (25)$$

Then, the smoothed spatial Fourier components are,

$$\overline{T}_a^{x}[(2k-1)\sigma] = H[(2k-1)\sigma]\,T_a^{x}[(2k-1)\sigma] \cdots\cdots\cdots\cdots (26)$$

for k=1, 2, ..., 2N,

3. Image Correction Procedure

The outputs from the two interferometer systems are recorded on a paper tape through an A-D converter. The A-D converter has eight input channels, and all the data are recorded at the same time (Tanaka, 1967). Total number of samples for one scan is 256, and the sampling interval is about 0.6 sec. This sampling interval is just one fourth of the theoretical maximum value for the adding interferometer and just a half of that for the compound interferometer. And this interval is changed according to the cosine of declination of the sun every day.

The flow chart of the data processing is shown in Fig. 2. Examples of a spatial frequency spectrum are shown in Figs. 3(a) and 3(b) (c. f., Fig. 2–1, 2), where it is clearly seen that their spectra are sharply cutoff at their theoretical maximum spatial frequencies. Restoration is carried out according to Eq. (22), and its examples are shown in Figs. 4(b), 5(b) and 6(b) (c. f., Fig. 2–3). Spatial Fourier components beyond the theoretical limit must be the noise independent of the source signal, so that these are cut from the spectra which may be called a kind of 'simulated spatial filtering'.

Odd spatial frequency harmonics of the restored brightness distribution of the sun are given by the Fourier transform of its alternately inverted solar scans, instead of the interpolation method of Eq. (23). Phase correction of the spatial frequency spectrum and the restoration of the fundamental spatial Fourier component for the

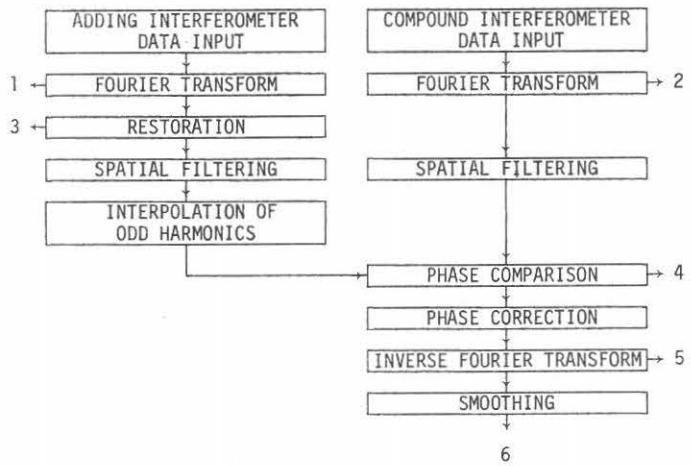

Fig. 2. Flow chart of image correction procedure (Numbers on the chart represent data outputs.).

9.4 GHz data are carried out by the method described in the previous section. After the inverse Fourier transform, the corrected image of the sun is obtained. The results of this procedure are shown in Figs. 4, 5 and 6 (c. f., Fig. 2–4, 5, 6), where the brightness distributions are normalized by the flux values obtained from single radiometer. In Figs. 4(f), 5(f), 6(f) and 7, phase differences between the two sets of spatial frequency spectra are shown, one is obtained from the compound interferometer and the other is from the adding interferometer after restoring.

From this we can estimate the phase error distribution along the antenna aperture to some extent. At higher spatial frequency region, where the S/N ratio is poor, this estimation is incorrect. So, these phase differences do not correspond to actual phase errors of antenna elements in higher spatial frequency region. This is evidently shown in Figs. 4(f), 5(f), 6(f) and 7, where the triangles which represent the values of estimated phase errors are scattered at higher spatial frequency region.

Owing to the Fast Fourier Transform algorithm, it takes only a few seconds to perform the Fourier transform of 512 samples. So, the computing time of this processing can be made as short as less than 20 seconds.

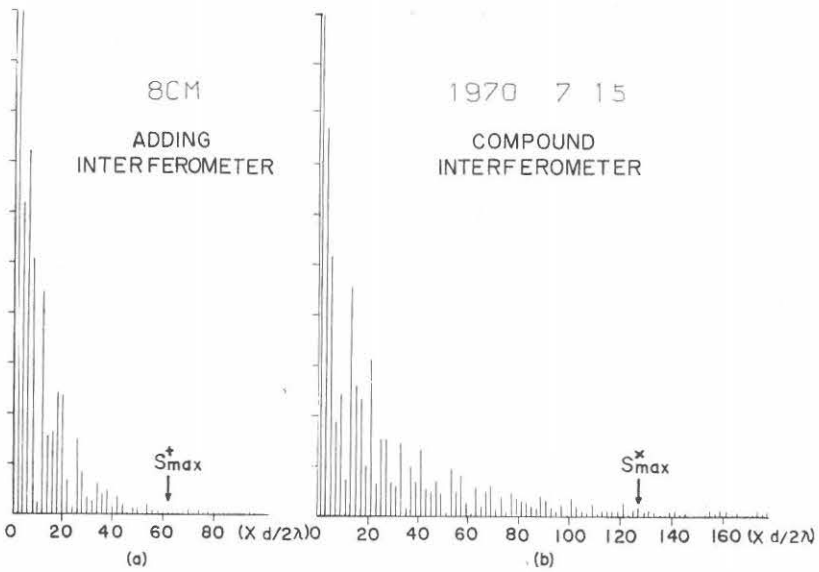

Fig. 3. Spatial frequency spectra of solar scans,

(a) observed with the adding interferometer at Toyokawa $[T_a^+(s)]$.

(b) observed with the compound interferometer at Toyokawa $[T_a^\times(s)]$.

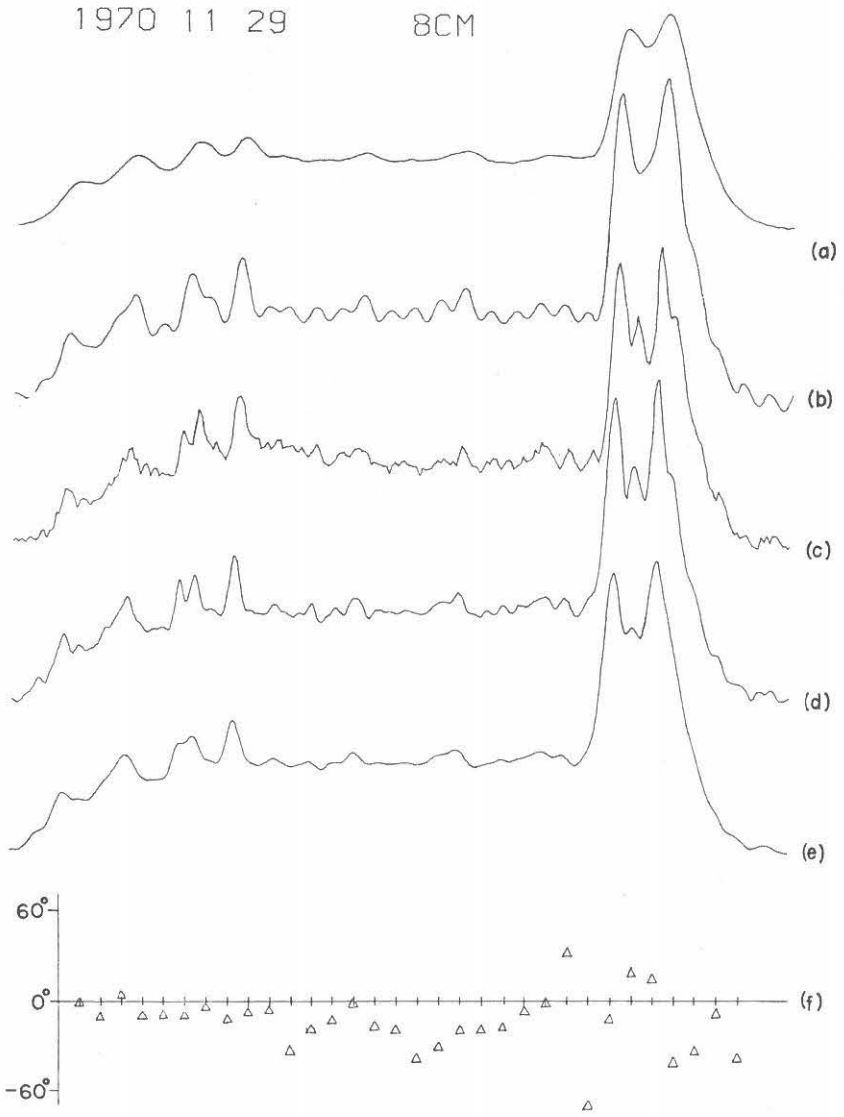

Fig. 4. The results of image correction at 3.75 GHz.

(a) A solar scan observed with the adding interferometer at Toyokawa $[T_a^+(u)]$.

(b) After filtering and restoring of (a) $[T_a^{+x}(u)]$.

(c) A solar scan observed with the compound interferometer at Toyokawa $[T_a^x(u)]$.

(d) After filtering and the phase correction of (c).

(e) After smoothing of (d).

(f) Estimated phase errors (The values are represented at the summits of triangles.).

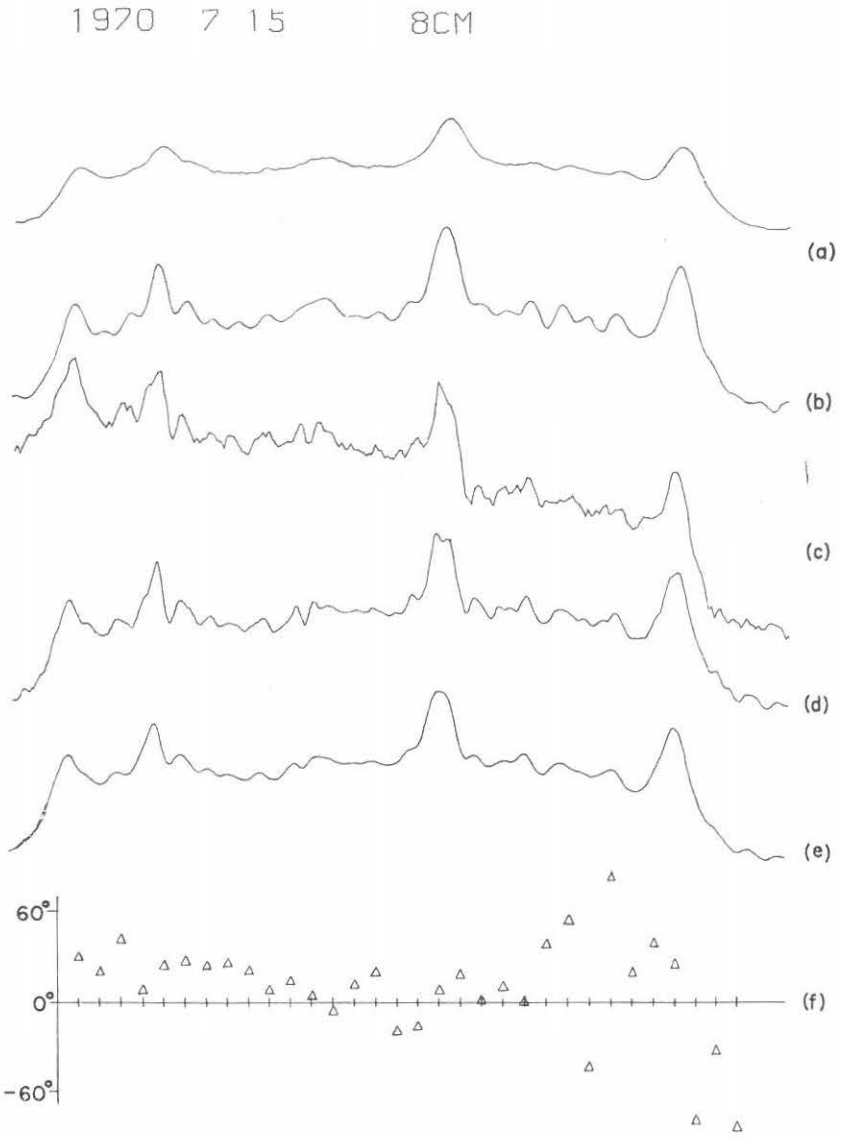

Fig. 5. The results of image correction at 3.75 GHz when there are remarkable phase errors (Explanations on (a), (b), (c), (d), (e) and (f) are quite same as in Fig. 4.).

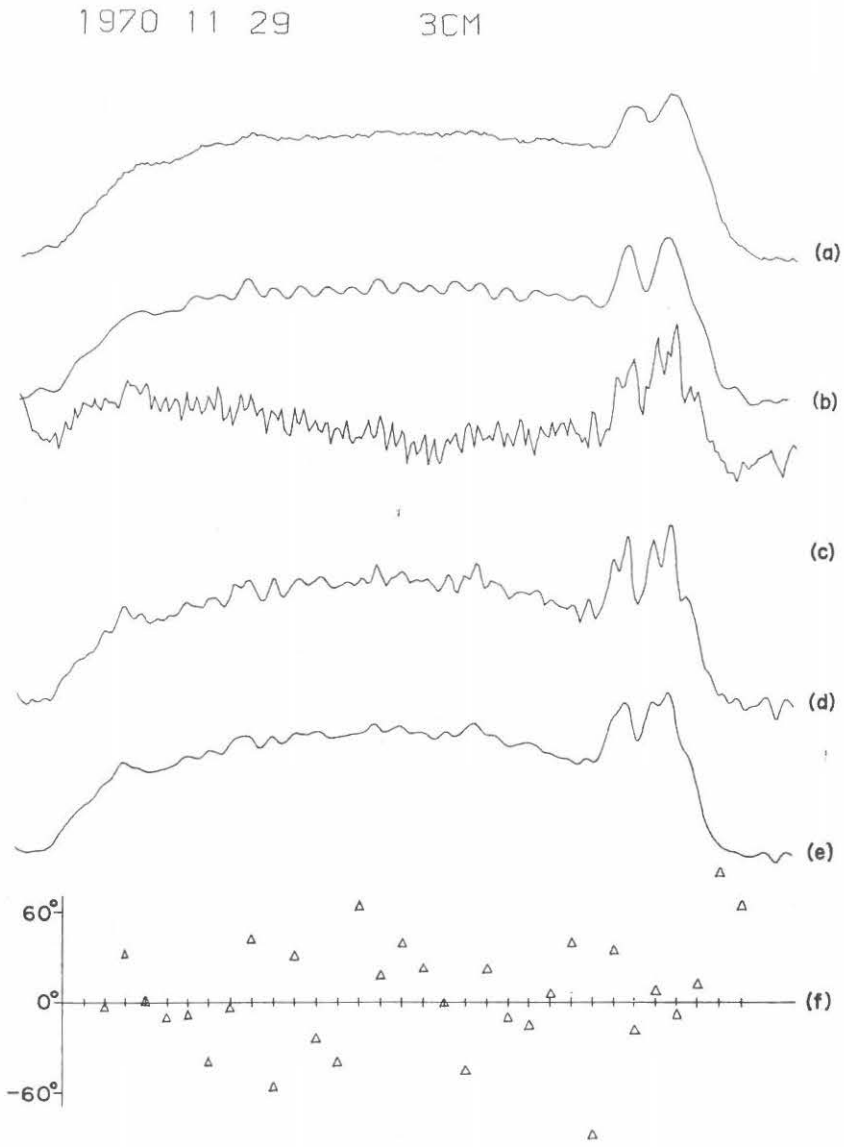

Fig. 6. The results of image correction at 9.4 GHz (Explanations on (a), (b), (c), (d), (e) and (f) are quite same as in Fig. 4.).

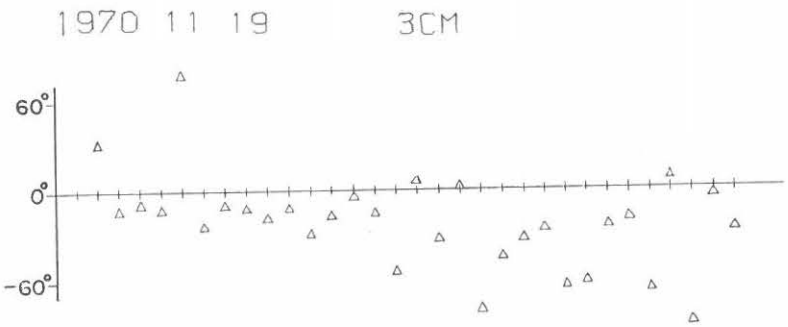

Fig. 7. Estimated phase errors when S/N ratio is good.

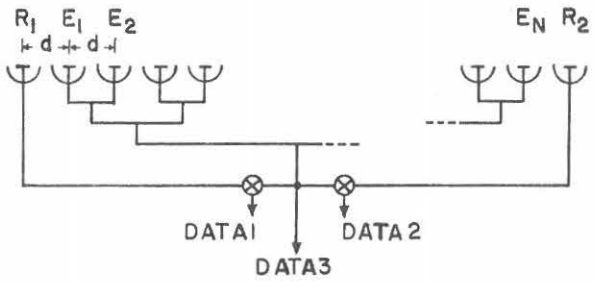

Fig. 8. The array configuration for the phase error correction by digital processing of 'DATA 1', 'DATA 2' and 'DATA 3'.

4. Future Problems

In previous discussion, we do not refer to the phase error correction in higher spatial frequency region for compound interferometer, where there are no corresponding spatial sensitivity in the adding interferometer. But, if we can make $\psi_1 = \psi_2 = 0$ in Eqs. (14) and (15), the phase of $s^x_{2(k+N)-1}$ has the same value as that of s^x_{2k-1} for $k=1, 2, \ldots, N$. Then it is possible to correct the phase errors of higher spatial Fourier components for compound interferometer, using the estimated phase error distribution obtained from lower spatial frequency spectra.

Further, it should be remembered that in multi-element interferometer of Fig. 1, where $D=d/2$ or $D=3d/2$, the spatial frequency spectrum obtained from compound interferometer is composed of odd harmonics only. while that from the adding interferometer is composed of even harmonics only. So, the comparison between the two

sets of the spatial frequency spectra can not be done directly.

In Fig. 8, a future proposal of the array configuration for the phase error correction is illustrated. In this system D=d and a pair of antenna elements R_1 and R_2 for phase error correction are set at both sides of the array.

So, direct comparison between spatial frequency spectra is possible without interpolation. The phase error distribution which is estimated from 'DATA 1' and 'DATA 3' is reliable at left-hand side of the array, on the other hand that from 'DATA 2' and 'DATA 3' is reliable at right-hand side of it.

Then the ambiguities in phase error estimation at higher spatial frequency region will be avoided by combining the two sets of estimated phase errors.

If this is done, more refined images of the sun will be obtained.

Acknowledgements

The auther wishes to express his sincere thanks to Prof. H. Tanaka, and Messrs. S. Énomé and M. Arisawa of Toyokawa Observatory for their valuable discussions. He thanks also Mr. T. Takayanagi and Miss K. Nakanishi for their assistance in data reduction.

References

Bracewell, R. N. Roberts, J. A.: Aerial Smoothing in Radio Astronomy, Aust. J. Phys., **7**, 615 (1954).

Bracewell, R. N.: Restoration in the Presence of Errors, Proc. I. R. E., **46**, No. 1, 106 (1958).

Burr, E. J.: Sharpening of Observational Data in Two Dimensions, Aust. J. Phys., **8**, 30 (1955).

Cooley, J. W. and Turkey, J. W.: An Algorithm for the Machine Calculation of Complex Fourier Series, Math. Comp., **19**, 297 (1965).

Ksienski, A.: Spatial Frequency Characteristics of Finite Aperture Antenna, Electromagnetic Theory and Antennas (E. C. Jordan, Ed.), Pergamon press, New York, N. Y., pt. 2, 1233 (1963).

Legg, T. H.: Smoothing for Phase-Switched Radio Telescopes, Proc. I. E. E. E. Trans., **AP -12**, 6, 803 (1964).

Peterson, C. E.: Correction of High-Resolution Solar Scans, Proc. ASA **1** (5) (1969).

Tanaka, H.: Toyokawa Observatory, Solar Physics, **1**, 295 (1967).

Tanaka, H., Kakinuma, T. and Énomé, S.: High-Resolution Observations of the Sources of Solar Radio Burst at 9.4 Gc/s, Proc. Res. Inst. Atmospherics, Nagoya Univ., **14**, 23 (1967).

Tanaka, H., Kakinuma, T., Énomé, S., Torii, C., Tsukiji, Y. and Kobayashi, S.: High-Resolution Quick-Scan Interferometer for Solar Studies at 3.75 GHz, ibid, **16**, 113 (1969).

Appendix

Fourier transform relations which characterize antenna observations are presented here,

(1) for the antenna

$$E(u) = \int_{-\infty}^{\infty} E(s) \exp(j2\pi su)\, ds \quad (A-1), \qquad E(s) = \int_{-\infty}^{\infty} E(u) \exp(-j2\pi su)\, du \quad (A-2),$$

$$P(u) = E(u) \cdot E(u)^* \quad (A-3), \qquad P(s) = \int_{-\infty}^{\infty} E(s'+s) \cdot E(s')^*\, ds' \quad (A-4),$$

$$P(u) = \int_{-\infty}^{\infty} P(s) \exp(j2\pi su)\, ds \quad (A-5), \qquad P(s) = \int_{-\infty}^{\infty} P(u) \exp(-j2\pi su)\, du \quad (A-6),$$

(2) for the radio source

$$T(u) = \int_{-\infty}^{\infty} T(s) \exp(j2\pi su)\, ds \quad (A-7), \qquad T(s) = \int_{-1}^{1} T(u) \exp(-j2\pi su)\, du \quad (A-8),$$

$$= \int_{-\infty}^{\infty} T(u) \exp(-j2\pi su)\, du \quad (A-9),$$

(if $T(u) = 0$ for $|u| > 1$)

(3) for the observable quantity

$$T_a(u) = \int_{-\infty}^{\infty} \tilde{P}(u-u') \cdot T(u')\, du' \quad (A-10), \qquad T_a(s) = \tilde{P}(s) \cdot T(s) \quad (A-11),$$

$$P(u) = P(-u) \quad (A-12), \qquad \tilde{P}(s) = P(-s) = P(s)^* \quad (A-13),$$

where,

u : a sine of the angle θ measured from the meridian plane (i. e., $u = \sin\theta$)

s : spatial frequency, that is the distance along the aperture measured in terms of wavelength λ ($s=x/\lambda$)

$E(u)$: far field pattern

$E(s)$: antenna aperture illumination

$P(u)$: antenna power pattern

$P(s)$: spatial frequency characteristics of an antenna

$T(u)$: original brightness distribution of the source

$T(s)$: spatial frequency spectrum of $T(u)$

$T_a(u)$: observed brightness distribution of the source

$T_a(s)$: spatial frequency spectrum of $T_a(u)$

and the symbol $*$ denotes the complex conjugate and the symbol $\tilde{}$ denotes the mirror image.